A Novel Anisotropic Hyper-viscoelastic Model for Predicting Fabric Draping Responses

Qingxuan Wei¹ and Dianyun Zhang²

School of Aeronautics and Astronautics, Purdue University, West Lafayette, Indiana, 47907-2045. USA

In Liquid Composite Molding (LCM), fabric draping determines the local fiber orientation which significantly affects the fabric permeability in the subsequent resin infusion and curing processes. This study aims to predict the deformation of multi-ply textile woven fabrics and the punch force during the fabric draping process through a hyper-viscoelastic constitutive modeling approach. Each ply of fabric is treated as a homogeneous anisotropic solid whose strain energy density function is developed based on a unit woven cell. The proposed constitutive model integrates fabric relaxation responses which have been clearly observed in the experiment. A generalized Maxwell model is used to simulate the evolution of nonequilibrium stresses generated during in-plane shear, transverse shear, and through-thickness compaction deformation. The proposed novel constitutive model was implemented in the commercial Finite Element Analysis (FEA) software Abaqus as a user-defined material subroutine, UMAT. Experiments including picture frame shear, cantilever beam bending, and through-thickness compaction tests were carried out to characterize the material properties of a sheet of fabric. The modeling approach was applied to simulate the fabric deformation response during a hemisphere draping process to demonstrate the predictive capability.

I. Introduction

Liquid Composite Molding (LCM) is widely recognized as a low-cost technology to produce complex-shaped fiber-reinforced polymer matrix composite products. In the beginning of the LCM, dry fiber preforms are draped over a mold, where the fabrics mainly undergo shearing and bending to conform to the surface of the mold. This draping process of textile preforms is critical to the subsequent resin infusion and curing processes and the resulting structural performance, since the local fiber orientation significantly affects the fabric permeability [1–4]. In addition, wrinkling can occur due to improperly designed mold geometry and the weak textile bending stiffness [5–8]. Hence, an efficient numerical model is needed to accurately capture the constitutive responses of textile woven fabrics and predict the fabric deformation during the draping process.

Diverse modeling approaches have been put forward in the literature to study the constitutive behavior of textile fibrous preforms. They can be classified into three main categories: discrete models, semi-discrete models, and continuum mechanics-based models. The discrete models describe the fabric textile architecture explicitly. A prevailing approach is Digital Fabric Mechanics Analyzer (DFMA) developed by Wang et al. [9,10], in which each fiber tow was simulated as a collection of digital chains. Each digital chain consists of multiple rod elements connected by frictionless pin-joints. The contact pairs between two nodes on the chains could be identified and an elastic element was assigned at each pair with its stiffness matrix controlling the sticking and sliding of the chains. Another popular approach is to model a fabric preform as a woven Unit Cell (UC) consisting of individual continuous yarns with circular, elliptical, or lenticular cross-sections [11–13]. The measuring of geometric parameters usually requires mesoscale images taken by a Scanning Electron Microscope. Commonly, the contact between the adjacent tows can be modeled through master/slave contact pairs and Coulomb friction using Finite Element Analysis (FEA). However,

¹ Graduate Student, School of Aeronautics and Astronautics.

² Assistant Professor, School of Aeronautics and Astronautics.

the vast degrees of freedom in FEA due to the complex textile fabric architecture limit the analysis of fabrics to small modeling domains, such as those to obtaining the effective properties of fabrics under periodic boundary conditions. To alleviate the problem, simplified geometries of fiber tows were invented in the literature[14–16]. For example, Gatouillat et al. [14] modeled each yarn as a series of flat shells whose geometric properties were characterized by fabric bending, shear, and tensile tests. In addition, the fiber tows can be modeled as beams [15,16]. Despite the simplified fabric architectures in FEA, the complex inter-tow contacts can still lead to high computational costs and possible convergence issues.

Semi-discrete models typically incorporate the fiber tow structures into user-defined elements in an FEA setting. Nguyen-Trong et al. [17] developed a user-defined four-node shell element based on the Mindlin plate theory, assuming that the material is orthotropic elastic. However, Bai et al. reported [18] that neither the Kirchhoff nor the Mindlin assumptions are appropriate for fibrous preforms since the assumptions relate the bending stiffness to the inplane elastic properties and the thickness of the material, which causes an overestimation of the bending stiffness. In Bai's approach, a triangular shell element was developed, whose virtual work includes terms for fiber tension, bending, and in-plane shear. Each term was computed by integrating the resultant, which is a polynomial function of its corresponding strain, with respect to the strain. Without the Kirchhoff or Mindlin assumptions, the displacement field was computed by nodal displacement increments, increments of nodal rotational angles, material normal, and material thickness. The curvature was calculated from the positions of neighboring elements. This approach worked well in predicting the fabric deformation, especially in tracking the material normal of thick fabrics. However, it is challenging to account for the through-thickness deformation in shell elements, limiting their use in flow-compaction analysis during the infusion and curing processes. Moreover, the implementation of user-defined elements can be burdensome, since it requires the generation of node lists, the mapping function, nodal forces and displacements, etc., leading to high barrier of entry.

Continuum mechanics-based models can alleviate the above-mentioned limitations of the discrete and semidiscrete methods. One or multiple layers of textile woven fabrics are modeled as a homogeneous ply whose constitutive law is determined from a UC. Hyperelastic models have been widely adopted based on the formation of strain energy density functions (SEDFs). A series of pseudo-invariants was defined as the double dot product of the right Cauchy-Green deformation tensor and a tensor that represents fiber directions [19,20]. In Charmetant's approach [19], the total SEDF was decomposed into the energy terms for some basic deformation modes: uniaxial tension, inplane shear, through-thickness compression, and transverse shear. Here, the fabric bending energy can be approximated by the effective tensile and transverse shear energy. The approach worked well in predicting the deformation of thin sheets of fabrics. When it comes to thick fabrics and the material normal is of interest, as discussed by Mathieu et al. [21], the bending energy should be formulated as a function of the second-order gradient of the displacement like the curvature.

As the textile fabrics are draped on a curved mold, axial forces result in the stretching and axial translation of fiber tows. Transverse forces can cause the bending, rotation, and transverse translation of the fiber tows. Sliding of fibers within a tow is also possible. At the macroscale, the displacement of the fiber tows is reflected as the bending, inplane shear, and the axial and transverse tension/compression of textile woven fabrics. Since the stiffness of fibers is considerably larger than the resistance to their movements, the axial deformation of fibers is limited. It is widely accepted that the in-plane shear and out-of-plane bending of fabrics dominate during the hemisphere draping process [22–24]. The through-thickness compaction should also be studied when the thickness change is important [25], especially for multi-ply fabrics. Therefore, the inter-tow and intra-tow frictions, which affect the relative movements of fibers, cause the time-dependent responses of dry fabrics during the in-plane shear, bending, and through-thickness compaction processes. More details of the experimental results can be found in Sec. III. However, these time-dependent responses have been seldomly considered in semi-discrete or continuum mechanics-based models.

In this paper, a novel anisotropic hyper-viscoelastic model is developed for dry textile fabrics based on the formation of an SEDF. The model features incorporation of the relaxation responses during the in-plane shear, transverse shear, and through-thickness compaction deformations through adding the nonequilibrium stresses of a Maxwell model to the total stresses. The predicted time-dependent deformation or force responses were compared to the results from the cantilever beam bending, picture frame shear, and through-thickness compaction experiments. Moreover, the proposed approach can be easily implemented in a commercial FEA software and the predictions can be completed accurately and efficiently (in three hours with one CPU).

The rest of the paper is organized as follows. The SEDF and the stresses are formulated in Sec. 2. Then, the experimental characterization of material properties is shown in Sec. 3, along with the details of the relaxation behaviors. Finally, the model is validated by a hemisphere draping simulation in FEA, which is shown in Sec. 4.

II. Modeling Approach for Woven Fabrics

In this section, an anisotropic hyper-viscoelastic model is developed for textile woven fabrics considering the energy dissipation during the in-plane shear, bending, and through-thickness compaction deformations. The focus is to add the nonequilibrium stresses, due to the energy dissipation, to the total stresses based on a Maxwell model.

A. Hyper-Viscoelastic Modeling Framework

A mesoscale UC of woven fabrics shown in Fig. 1 is homogenized as a continuous transversely isotropic hyperelastic material whose SEDF, denoted as W, can be divided into two parts: an elastic part W_e and a viscous part W_v as

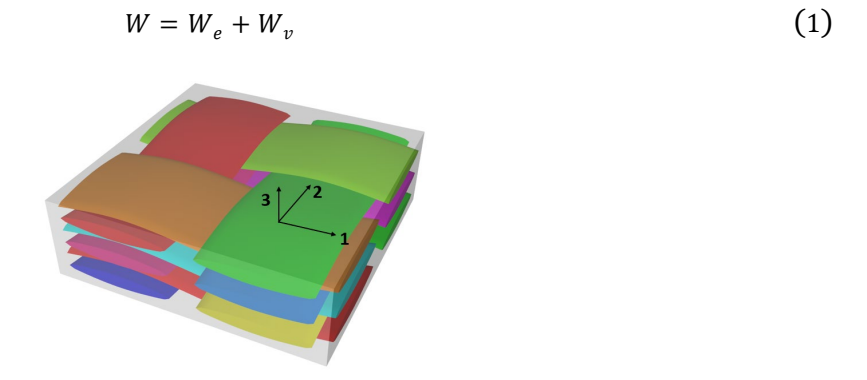


Fig. 1 A UC of woven fabrics.

It is assumed that any complex deformation can be decomposed into six basic modes: tension/compression in the 1-, 2-, and 3-directions, as well as the shear in the 1-2, 1-3, and 2-3 planes. Define the pseudo-invariants to represent the large deformation as

$$I_4^{ij} = (A^i)^T \cdot \mathbf{C} \cdot A^j \tag{2}$$

where i and j are both 3 in a three-dimensional analysis. C is the right Cauchy-Green deformation tensor computed from $C = F^T F$. The deformation gradient matrix F is defined as $F = \frac{\partial x}{\partial X}$, where x is the position in the deformed configuration and X is the position in the reference configuration. A^i are the vectors pointing in the directions of interest. Here, A^1 and A^2 represent the orientations of the warp and weft tows, and A^3 dictates the through-thickness direction. Due to the symmetry of C, there are only six independent pseudo-invariants: I_4^{11} , I_4^{22} , I_4^{33} , I_4^{12} , I_4^{13} , and I_4^{23} . The elastic part of the SEDF for normal behaviors can be related to I_4^{11} , I_4^{22} , and I_4^{33} , since they are the square of the stretch λ_i along each direction of interest, expressed as

$$I_4^{ii} = \left(A^{(i)}\right)^T \cdot \boldsymbol{C} \cdot A^{(i)} = \lambda_i^2$$
 ignoring the dummy index (3)

The SEDF for shear deformations can be related to the sinusoidal function of the shear angles γ as

$$\sin \gamma_{ij} = \frac{I_4^{ij}}{\sqrt{I_4^{ii}I_4^{ij}}}$$
 ignoring the dummy index (4)

Therefore, the expression of W_e can be developed as

$$W^e = W_f^e + W_t^e + W_{ts}^e + W_s^e (5)$$

where W_f^e represents the SEDF due to the stretch of fibers, W_t^e is the SEDF caused by the tension or compaction along the thickness direction, W_{ts}^e is the SEDF for transverse shear, and W_s^e is the SEDF for in-plane shear. They can be expressed in Eqs. 6-9.

$$W_f^e = \frac{E_{f1}}{2} (I_4^{11} - 1)^2 + \frac{E_{f2}}{2} (I_4^{22} - 1)^2$$
 (6)

$$W_t^e = \frac{E_t}{2} (I_4^{33} - 1)^2 \tag{7}$$

$$W_{ts}^{e} = \frac{E_{ts}}{2} \left(\frac{I_{4}^{13}}{\sqrt{I_{4}^{11} I_{4}^{33}}} - \xi_{13} \right)^{2} + \frac{E_{ts}}{2} \left(\frac{I_{4}^{23}}{\sqrt{I_{4}^{22} I_{4}^{33}}} - \xi_{23} \right)^{2}$$
 (8)

$$W_s^e = \frac{E_s}{2} \left(\frac{I_4^{12}}{\sqrt{I_4^{11} I_4^{22}}} - \xi_{12} \right)^n \tag{9}$$

where E_{f1} and E_{f2} are the moduli controlling the fiber tension. For a transversely isotropic material, $E_{f1} = E_{f2} = E_f$. Different values for E_f can be assigned when the material is under tension and compression as

$$E_f = \begin{cases} E_{ten} & ifI_4^{11} \ orI_4^{22} \ge 1 \\ E_{comp} & ifI_4^{11} \ orI_4^{22} < 1 \end{cases}$$
 (10)

 E_{ts} is the modulus that controls the transverse shear behavior. ξ_{ij} is the initial value of $\sin \gamma_{ij}$. The bending energy is approximated by the axial tension energy W_f^e and transverse shear energy W_{ts}^e . Since the out-of-plane bending behavior is more critical than the stretch of fibers during the draping process, E_f and E_{ts} are determined by the bending responses. E_t is the modulus that controls the through-thickness tension and compression. E_s is the modulus that controls the in-plane shear behavior. Note that the power of the in-plane shear term in Eq. 9 is also a variable n due to the highly nonlinear characteristic of the in-plane shear behavior of textile fabrics. Then, the equilibrium second Piola-Kirchhoff stress can be computed as

$$S^{\alpha} = 2 \frac{\partial W_{\alpha}^{e}}{\partial C}, \qquad \alpha = f, t, ts, s$$
 (11)

where α represents the deformation mode.

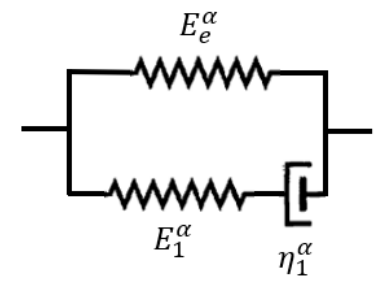


Fig. 2 Illustration of the linear Maxwell model.

The viscous energy includes the energy for the in-plane shear W_s^v , transverse shear W_{ts}^v , and through-thickness compaction W_t^v .

$$W^{v} = W_{s}^{v} + W_{ts}^{v} + W_{t}^{v} \tag{12}$$

Since this only describes the energy that can be fully dissipated after relaxation and no time-dependent characteristic is included, an extra model is needed to simulate the evolution of nonequilibrium stresses Q^{α} . Here, a linear Maxwell model incorporating one elastic element and one Maxwell element, shown in Fig. 2, is adopted to capture the evolution of Q^{α} as

$$\dot{\mathbf{Q}}^{\alpha} + \frac{\mathbf{Q}^{\alpha}}{\tau_{\alpha}} = \dot{\mathbf{P}}^{\alpha} \tag{13}$$

where \mathbf{P}^{α} is the second Piola-Kirchhoff stress carried by the spring in the Maxwell arm; the relaxation time $\tau_{\alpha} = \frac{\eta_{1}^{\alpha}}{E_{1}^{\alpha}}$; $\mathbf{\dot{Q}}^{\dot{\alpha}} = \frac{d\mathbf{\dot{Q}}^{\alpha}}{dt}$; $\mathbf{\dot{P}}^{\dot{\alpha}} = \frac{d\mathbf{\dot{P}}^{\alpha}}{dt}$; and α can be t, ts, and s. Further, assume that $\mathbf{\dot{P}}^{\alpha}$ is proportional to $\mathbf{\dot{S}}^{\alpha}$ and the ratio is denoted as a constant β_{α} . It also depicts the ratio of the viscous energy to the elastic energy.

$$\frac{\mathbf{P}^{\alpha}}{\mathbf{S}^{\alpha}} = \frac{E_{1}^{\alpha}}{E_{e}^{\alpha}} = \frac{W_{\alpha}^{\nu}}{W_{\alpha}^{e}} = \beta_{\alpha} \tag{14}$$

Then, the evolution of Q^{α} can be computed by solving the ordinary differential equation.

$$\dot{\mathbf{Q}}^{\alpha} + \frac{\mathbf{Q}^{\alpha}}{\tau_{\alpha}} = \beta_{\alpha} \dot{\mathbf{S}}^{\alpha} \tag{15}$$

The total second Piola-Kirchhoff stress is,

$$\mathbf{S} = \mathbf{S}^f + \mathbf{S}^s + \mathbf{S}^{ts} + \mathbf{S}^t + \mathbf{Q}^s + \mathbf{Q}^{ts} + \mathbf{Q}^t$$
 (16)

and the total Cauchy stress is

$$\sigma = \frac{1}{J} F S F^T \tag{17}$$

More details regarding the derivation can be found in Sec. B.

B. Numerical Implementation

The model was implemented in Abaqus via UMAT user-subroutine. This section shows the derivations of the Cauchy stresses and the consistent Jacobian which are required to be updated in the UMAT.

1. Stresses

In order to compute the Cauchy stresses, the equilibrium and nonequilibrium second order Piola-Kirchhoff stresses are needed according to Eq. 16. The equilibrium second order Piola-Kirchhoff stress for the tension/compression is derived as

$$S^{f} = 2 \frac{\partial W_{f}^{e}}{\partial C} = 2E_{f1}(I_{4}^{11} - 1) \frac{\partial I_{4}^{11}}{\partial C} + 2E_{f2}(I_{4}^{22} - 1) \frac{\partial I_{4}^{22}}{\partial C}$$
(18)

The equilibrium second order Piola-Kirchhoff stress for the through-thickness behavior is related to I_4^{33} .

$$S^{t} = 2 \frac{\partial W_{t}^{e}}{\partial \mathbf{c}} = 2 \frac{\partial \left[\frac{E_{t}}{2} (I_{4}^{33} - 1)^{2} \right]}{\partial I_{4}^{33}} \frac{\partial I_{4}^{33}}{\partial \mathbf{c}} = 2E_{t} (I_{4}^{33} - 1) \frac{\partial I_{4}^{33}}{\partial \mathbf{c}}$$
(19)

The equilibrium second order Piola-Kirchhoff stress for the in-plane shear is

$$S^{s} = 2 \frac{\partial W_{s}^{e}}{\partial C} = 2 \left(\frac{\partial W_{s}^{e}}{\partial I_{4}^{11}} \frac{\partial I_{4}^{11}}{\partial C} + \frac{\partial W_{s}^{e}}{\partial I_{4}^{22}} \frac{\partial I_{4}^{22}}{\partial C} + \frac{\partial W_{s}^{e}}{\partial I_{4}^{12}} \frac{\partial I_{4}^{12}}{\partial C} \right)$$

$$= \left[\frac{nE_{s}}{\sqrt{I_{4}^{11}I_{4}^{22}}} \cdot \frac{\partial I_{4}^{12}}{\partial C} - \frac{nE_{s}I_{4}^{12}I_{4}^{22}}{2(I_{4}^{11}I_{4}^{22})^{\frac{3}{2}}} \cdot \frac{\partial I_{4}^{11}}{\partial C} - \frac{nE_{s}I_{4}^{12}I_{4}^{11}}{2(I_{4}^{11}I_{4}^{22})^{\frac{3}{2}}} \cdot \frac{\partial I_{4}^{22}}{\partial C} \right] r_{1}^{n-1}$$
(20)

$$r_1 = \frac{I_4^{12}}{\sqrt{I_4^{11}I_4^{22}}} - \xi_{12} \tag{21}$$

The equilibrium second order Piola-Kirchhoff stress for the transverse shear is

$$S^{ts} = 2 \frac{\partial W_{ts}^{e}}{\partial \mathbf{C}} = 2 \left(\frac{\partial W_{ts}^{e}}{\partial I_{4}^{11}} \frac{\partial I_{4}^{11}}{\partial \mathbf{C}} + \frac{\partial W_{ts}^{e}}{\partial I_{4}^{22}} \frac{\partial I_{4}^{22}}{\partial \mathbf{C}} + \frac{\partial W_{ts}^{e}}{\partial I_{4}^{33}} \frac{\partial I_{4}^{33}}{\partial \mathbf{C}} + \frac{\partial W_{ts}^{e}}{\partial I_{4}^{13}} \frac{\partial I_{4}^{13}}{\partial \mathbf{C}} + \frac{\partial W_{ts}^{e}}{\partial I_{2}^{23}} \frac{\partial I_{4}^{33}}{\partial \mathbf{C}} \right)$$

$$= \left[2 \frac{E_{ts}}{\sqrt{I_{4}^{11}I_{4}^{33}}} \frac{\partial I_{4}^{13}}{\partial \mathbf{C}} - \frac{E_{ts}I_{4}^{13}I_{4}^{33}}{(I_{4}^{11}I_{4}^{33})^{\frac{3}{2}}} \frac{\partial I_{4}^{11}}{\partial \mathbf{C}} - \frac{E_{ts}I_{4}^{13}I_{4}^{13}}{(I_{4}^{11}I_{4}^{33})^{\frac{3}{2}}} \frac{\partial I_{4}^{33}}{\partial \mathbf{C}} \right] r_{2}$$

$$+ \left[2 \frac{E_{ts}}{\sqrt{I_{4}^{22}I_{4}^{33}}} \frac{\partial I_{4}^{23}}{\partial \mathbf{C}} - \frac{E_{ts}I_{4}^{23}I_{4}^{33}}{(I_{4}^{22}I_{4}^{33})^{\frac{3}{2}}} \frac{\partial I_{4}^{22}}{\partial \mathbf{C}} - \frac{E_{ts}I_{4}^{23}I_{4}^{23}}{(I_{4}^{22}I_{4}^{33})^{\frac{3}{2}}} \frac{\partial I_{4}^{33}}{\partial \mathbf{C}} \right] r_{3}$$

$$(22)$$

$$r_2 = \frac{I_4^{13}}{\sqrt{I_4^{11}I_4^{33}}} - \xi_{13} \tag{23}$$

$$r_3 = \frac{I_4^{23}}{\sqrt{I_4^{22}I_4^{33}}} - \xi_{23} \tag{24}$$

In Eqs. 18-24, $\frac{\partial I_4^{ij}}{\partial c} = \frac{1}{2} (A_i \otimes A_j + A_j \otimes A_i) = \mathbf{M}^k$, where k = i, if i = j; and k = i + j + 1, if $i \neq j$. This tensor will be further used in the derivation of the consistent Jacobian.

Next, the nonequilibrium second Piola-Kirchhoff stresses are derived in an incremental form. The central difference scheme is used.

$$\dot{f}_{t+\frac{1}{2}\Delta t} = \frac{\Delta f}{\Delta t} \tag{25}$$

$$f_{t+\frac{1}{2}\Delta t} = f_t + \frac{\Delta f}{2} \tag{26}$$

where f represents a variable and t is time. Then, the ordinary differential equations for the nonequilibrium stresses become

$$\dot{\mathbf{Q}}^{\alpha} + \frac{\mathbf{Q}^{\alpha}}{\tau_{\alpha}} = \beta_{\alpha} \dot{\mathbf{S}}^{\alpha} \tag{27}$$

$$\frac{\boldsymbol{Q}^{\alpha}|_{t+\Delta t} - \boldsymbol{Q}^{\alpha}|_{t}}{\Delta t} + \frac{\boldsymbol{Q}^{\alpha}|_{t} + \frac{\boldsymbol{Q}^{\alpha}|_{t+\Delta t} - \boldsymbol{Q}^{\alpha}|_{t}}{2}}{\tau_{\alpha}} = \beta_{\alpha} \frac{\boldsymbol{S}^{\alpha}|_{t+\Delta t} - \boldsymbol{S}^{\alpha}|_{t}}{\Delta t}$$
(28)

where α can be s, ts, and t. $\boldsymbol{Q}^{\alpha}|_{t+\Delta t}$ can be solved as

$$\boldsymbol{Q}^{\alpha}|_{t+\Delta t} = \left(1 - \frac{2\Delta t}{2\tau_{\alpha} + \Delta t}\right) \boldsymbol{Q}^{\alpha}|_{t} + \frac{2\tau_{\alpha}}{2\tau_{\alpha} + \Delta t} \beta_{\alpha} (\boldsymbol{S}^{\alpha}|_{t+\Delta t} - \boldsymbol{S}^{\alpha}|_{t})$$
(29)

2. The Consistent Jacobian

In the UMAT, the consistent Jacobian also needs to be provided, which is defined as the derivative of the Jaumann rate of the Kirchhoff stress with respect to the deformation rate D_{IJ} . The consistent Jacobian without the consideration of viscous effects is related to the Jaumann rate of the elastic Kirchhoff stress τ_{ij}^{θ} and it can be simplified into [26]:

$$\mathbb{C}_{ijIJ}^{e} = \frac{\partial \tau_{ij}^{\theta}}{\partial D_{IJ}} = \frac{1}{2} \left(\delta_{iI} \sigma_{jj}^{e} + \delta_{iJ} \sigma_{jl}^{e} + \sigma_{iI}^{e} \delta_{jJ} + \sigma_{iJ}^{e} \delta_{jI} \right) + \frac{1}{J} \left(\delta_{II} \delta_{hJ} + \delta_{IJ} \delta_{hI} \right) F_{im} F_{jn} F_{hp} F_{lq} \frac{\partial S_{mn}}{\partial C_{pq}}$$
(30)

The Cauchy stresses in the first part of \mathbb{C}_{ijIJ}^e are derived in Sec. B.1., so the key component of the second part $\frac{\partial S_{mn}}{\partial C_{pq}}$ is provided here, where \mathbf{M}^k is the tensor mentioned in Sec. B.1.

$$\frac{\partial S_{mn}}{\partial C_{pq}} = 2E_{f1}M_{mn}^1M_{pq}^1 + 2E_{f2}M_{mn}^2M_{pq}^2 + \frac{\partial S_{mn}^s}{\partial C_{pq}} + \frac{\partial S_{mn}^{ts}}{\partial C_{pq}} + \frac{\partial S_{mn}^{ts}}{\partial C_{pq}}$$
(31)

Here, the term $\frac{\partial S_{mn}^{s}}{\partial c_{pq}}$ is for the in-plane shear behavior, expressed as

$$\frac{\partial S_{mn}^s}{\partial C_{pq}} = M_{mn}^4 T_{pq}^1 + M_{mn}^1 T_{pq}^2 + M_{mn}^2 T_{pq}^3$$
 (32)

where

$$T^{1} = \frac{E_{s}n(n-1)r_{1}^{n-2}}{\sqrt{I_{4}^{11}I_{4}^{22}}}H^{1} - \frac{E_{s}n\,r_{1}^{n-1}}{2\sqrt{I_{4}^{11}I_{4}^{22}}}\left(\frac{M^{1}}{I_{4}^{11}} + \frac{M^{2}}{I_{4}^{22}}\right)$$
(33)

$$T^{2} = E_{s} n \, r_{1}^{n-1} \left[\frac{3I_{4}^{12} \mathbf{M}^{1}}{4(I_{4}^{11})^{2} \sqrt{I_{4}^{11} I_{4}^{22}}} + \frac{I_{4}^{12} \mathbf{M}^{2}}{4(I_{4}^{11} I_{4}^{22})^{\frac{3}{2}}} - \frac{\mathbf{M}^{4}}{2I_{4}^{11} \sqrt{I_{4}^{11} I_{4}^{22}}} \right] - \frac{E_{s} n(n-1)I_{4}^{12} r_{1}^{n-2}}{2I_{4}^{11} \sqrt{I_{4}^{11} I_{4}^{22}}} \mathbf{H}^{1}$$
(34)

$$T^{3} = E_{s} n \, r_{1}^{n-1} \left[\frac{3I_{4}^{12} \mathbf{M}^{2}}{4(I_{4}^{22})^{2} \sqrt{I_{4}^{11} I_{4}^{22}}} + \frac{I_{4}^{12} \mathbf{M}^{1}}{4(I_{4}^{11} I_{4}^{22})^{\frac{3}{2}}} - \frac{\mathbf{M}^{4}}{2I_{4}^{22} \sqrt{I_{4}^{11} I_{4}^{22}}} \right] - \frac{E_{s} n(n-1)I_{4}^{12} r_{1}^{n-2}}{2I_{4}^{22} \sqrt{I_{4}^{11} I_{4}^{22}}} \mathbf{H}^{1}$$
(35)

$$H^{1} = \frac{M^{4}}{\sqrt{I_{4}^{11}I_{4}^{22}}} - \frac{I_{4}^{12}}{2\sqrt{I_{4}^{11}I_{4}^{22}}} \left(\frac{M^{1}}{I_{4}^{11}} + \frac{M^{2}}{I_{4}^{22}}\right)$$
(36)

The term $\frac{\partial S_{mn}^{ts}}{\partial c_{pq}}$ is for the transverse shear behavior, and written as

$$\frac{\partial S_{mn}^{cs}}{\partial C_{pq}} = M_{mn}^5 T_{pq}^4 + M_{mn}^1 T_{pq}^5 + M_{mn}^3 T_{pq}^6 + M_{mn}^6 T_{pq}^7 + M_{mn}^2 T_{pq}^8 + M_{mn}^3 T_{pq}^9$$
(37)

$$T^{4} = 2E_{ts} \left[\frac{H^{2}}{\sqrt{I_{A}^{11} I_{A}^{33}}} - \frac{r_{2}}{2\sqrt{I_{A}^{11} I_{A}^{33}}} \left(\frac{M^{1}}{I_{4}^{11}} + \frac{M^{3}}{I_{4}^{33}} \right) \right]$$
(38)

$$T^{5} = 2E_{ts}r_{2} \left[\frac{3I_{4}^{13}\mathbf{M}^{1}}{4(I_{4}^{11})^{2}\sqrt{I_{4}^{11}I_{4}^{33}}} + \frac{I_{4}^{13}\mathbf{M}^{3}}{4(I_{4}^{11}I_{4}^{33})^{\frac{3}{2}}} - \frac{\mathbf{M}^{5}}{2I_{4}^{11}\sqrt{I_{4}^{11}I_{4}^{33}}} \right] - \frac{E_{ts}I_{4}^{13}}{I_{4}^{11}\sqrt{I_{4}^{11}I_{4}^{33}}} \mathbf{H}^{2}$$
(39)

$$T^{6} = 2E_{ts}r_{2} \left[\frac{3I_{4}^{13}\mathbf{M}^{3}}{4(I_{4}^{33})^{2}\sqrt{I_{4}^{11}I_{4}^{33}}} + \frac{I_{4}^{13}\mathbf{M}^{1}}{4(I_{4}^{11}I_{4}^{33})^{\frac{3}{2}}} - \frac{\mathbf{M}^{5}}{2I_{4}^{33}\sqrt{I_{4}^{11}I_{4}^{33}}} \right] - \frac{E_{ts}I_{4}^{13}}{I_{4}^{33}\sqrt{I_{4}^{11}I_{4}^{33}}} \mathbf{H}^{2}$$

$$(40)$$

$$T^{7} = 2E_{ts} \left[\frac{H^{3}}{\sqrt{I_{4}^{22}I_{4}^{33}}} - \frac{r_{3}}{2\sqrt{I_{4}^{22}I_{4}^{33}}} \left(\frac{M^{2}}{I_{4}^{2}} + \frac{M^{3}}{I_{4}^{33}} \right) \right]$$
(41)

$$T^{8} = 2E_{ts}r_{3} \left[\frac{3I_{4}^{23}\mathbf{M}^{2}}{4(I_{4}^{22})^{2}\sqrt{I_{4}^{22}I_{4}^{33}}} + \frac{I_{4}^{23}\mathbf{M}^{3}}{4(I_{4}^{22}I_{4}^{33})^{\frac{3}{2}}} - \frac{\mathbf{M}^{6}}{2I_{4}^{22}\sqrt{I_{4}^{22}I_{4}^{33}}} \right] - \frac{E_{ts}I_{4}^{23}}{I_{4}^{22}\sqrt{I_{4}^{22}I_{4}^{33}}} H^{3}$$

$$(42)$$

$$T^{9} = 2E_{ts}r_{3} \left[\frac{3I_{4}^{23}\mathbf{M}^{3}}{4(I_{4}^{33})^{2}\sqrt{I_{4}^{22}I_{4}^{33}}} + \frac{I_{4}^{23}\mathbf{M}^{2}}{4(I_{4}^{22}I_{4}^{33})^{\frac{3}{2}}} - \frac{\mathbf{M}^{6}}{2I_{4}^{33}\sqrt{I_{4}^{22}I_{4}^{33}}} \right] - \frac{E_{ts}I_{4}^{23}}{I_{4}^{33}\sqrt{I_{4}^{22}I_{4}^{33}}} \mathbf{H}^{2}$$

$$(43)$$

$$H^{2} = \frac{M^{5}}{\sqrt{I_{4}^{11}I_{4}^{33}}} - \frac{I_{4}^{13}}{2\sqrt{I_{4}^{11}I_{4}^{33}}} \left(\frac{M^{1}}{I_{4}^{11}} + \frac{M^{3}}{I_{4}^{33}}\right)$$
(44)

$$H^{3} = \frac{M^{6}}{\sqrt{I_{4}^{22}I_{4}^{33}}} - \frac{I_{4}^{23}}{2\sqrt{I_{4}^{22}I_{4}^{33}}} \left(\frac{M^{2}}{I_{4}^{22}} + \frac{M^{3}}{I_{4}^{33}}\right)$$
(45)

Since the viscous energy has been linked to the elastic energy by an energy ratio β_{α} , the viscous part of the consistent Jacobian can also be added through another non-dimensional ratio δ_{α} as [27]

$$\mathbb{C}_{ijIJ} = \mathbb{C}_{ijIJ}^e + \sum_{\alpha} \delta_{\alpha} \mathbb{C}_{ijIJ}^{\alpha} \tag{46}$$

$$\delta_{\alpha} = \frac{2\tau_{\alpha}}{2\tau_{\alpha} + \Delta t} \beta_{\alpha} \tag{47}$$

 $\mathbb{C}_{ijIJ}^{\alpha}$ is the elastic part of the consistent Jacobian for the deformation mode α , and α can be t, ts, and s. $\mathbb{C}_{ijIJ}^{\alpha}$ is expressed as

$$\mathbb{C}_{ijIJ}^{\alpha} = \frac{1}{2} \left(\delta_{iI} \sigma_{JJ}^{\alpha} + \delta_{iJ} \sigma_{JI}^{\alpha} + \sigma_{iI}^{\alpha} \delta_{JJ} + \sigma_{iJ}^{\alpha} \delta_{JI} \right) + \frac{1}{I} \left(\delta_{II} \delta_{hJ} + \delta_{IJ} \delta_{hI} \right) F_{im} F_{jn} F_{hp} F_{lq} \frac{\partial S_{mn}^{\alpha}}{\partial C_{nq}}$$

$$\tag{48}$$

In this equation, $\frac{\partial S_{mn}^{\alpha}}{\partial C_{pq}}$ is already provided and $\sigma^{\alpha} = \frac{1}{J}FS^{\alpha}F^{T}$.

III. Material Properties Characterization

The characterization of mechanical properties of a single layer of T300 carbon fiber plain weave fabric is presented in this section. The out-of-plane bending, and in-plane shear properties were characterized by cantilever beam bending and picture frame tests on a layer of fabric. Through-thickness compaction tests were conducted for multi-ply fabrics to obtain the compaction properties. Fabric relaxation behaviors show up distinctly in the history of deflections or reaction forces during these tests.

A. Bending Behaviors

Fabrics of 7.62×12 cm and 7.62×15 cm were clamped at the left end and suspended at the right end (see Fig. 3 (a)). A 5 cm grid was drawn at the background plate. Deformed shapes at different times were recorded by a camera. The deflections in the photos were measured using image analysis software, ImageJ, using the background gridlines as the references. Three tests for each specimen were conducted, and the average deflection was obtained and plotted in Fig. 4.

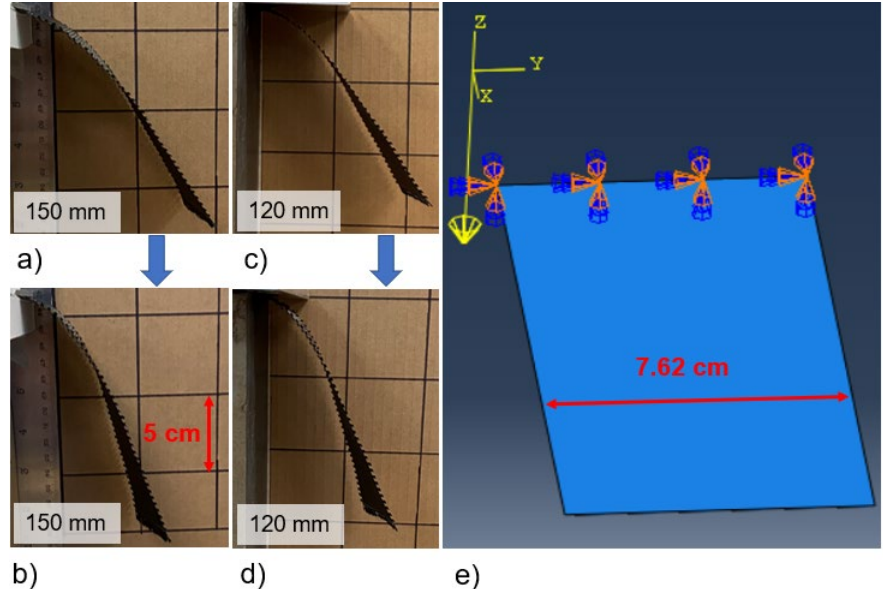


Fig. 3 The bended fabrics of the (a) 150 mm fabric before relaxation, (b) 150 mm fabric after relaxation, (c) 120 mm fabric before relaxation, (d) 120 mm fabric after relaxation in the cantilever bending tests; (e) the bending model in Abaqus consisting of a fabric fixed at one end and hanging at the other end under the gravity along -z direction.

The area density, ρ_{area} , and thickness, h, of a single ply of the carbon fabric were measured. The results were: $\rho_{area} = 0.219 \text{ kg/m}^2$ and h = 0.250 mm. The fabric density can be computed as

$$\rho = \frac{\rho_{area}}{h} = 0.876 \ kg/m^3 \tag{49}$$

The density was inputted into a corresponding bending model built in Abaqus (Fig. 3 (e)). Single plies of fabrics were created in size to the specimens in the experiments. One end of the ply was fixed, and the other end was draped by the materials' own weight. The deflection of the fabrics vs. time responses in the model are shown in Fig. 4. The bending properties in Table 1 were tuned until the predicted deflection curves closely approximated the experimentally measured ones.

Table 1. Material properties that control the bending behavior

ρ (kg/m ³)	E _{ten} (MPa)	E _{comp} (MPa)	E _{ts} (MPa)	$oldsymbol{eta}_{ts}$	$ au_{ts}$ (min)
0.87576	80	10	1.8	0.75	40

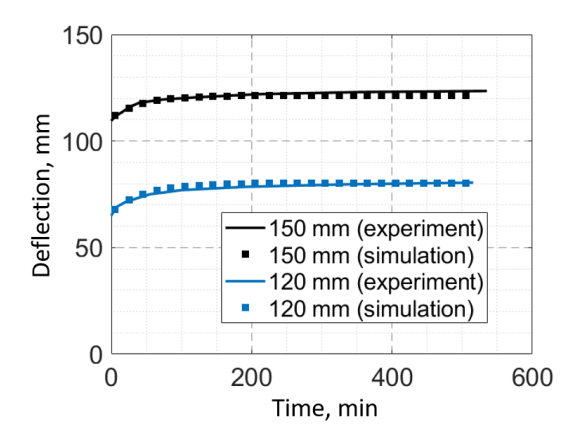


Fig. 4 The deflection vs. time responses from experiments and simulations.

B. In-plane Shear Behaviors

a)

b)

This section summarizes the characterization of the in-plane shear properties of woven fabrics. Picture frame tests were conducted to capture the shear force vs. shear angle responses, and a picture frame test model was built in Abaqus. The experimental and numerical results were compared to obtain the proper values of in-plane shear properties.

1. Picture frame tests

The picture frame test is a common approach to study the behavior of fabrics subject to in-plane shear loading. A sample of carbon fabric was clamped in a metal picture frame as shown in Fig. 5 (a), which is made of four pairs of metal bars pinned at the ends. The metal frame was mounted on a tension test machine. Initially, the angle between the warp and weft tows was set to 90° using a square. As the test started, the top crosshead was fixed, and the bottom crosshead moved downwards at 35 mm/min for 96 mm. Then, the bottom crosshead rested for 3 minutes before moving back at 35 mm/min to the initial position. Time, as well as the force and displacements of the bottom crosshead were recorded during the tests. The initial force and displacement were both set to zero. The shear angle γ is an important parameter that describes the in-plane shear behavior which is commonly defined as the change of the angle between the warp and weft yarns [28–37]. As illustrated in Fig. 5 (b), γ can be computed from the displacement of the crosshead d and the length of the frame L_{frame} according to Eqs. 50 - 51 [36].

$$\gamma = \frac{\pi}{2} - 2\theta \tag{50}$$

$$\theta = acos\left(\frac{\sqrt{2}L_{frame} + d}{2L_{frame}}\right) (Ref. [3])$$

$$(51)$$

$$\frac{\sqrt{2}L_{frame}}{\sqrt{2}L_{frame}} = \frac{\sqrt{2}L_{frame}}{\sqrt{2}L_{frame}} = \frac{\sqrt{2}$$

c)

Fig. 5 (a) The setup of picture frame test and the deformed real fabric when shear angle $\gamma = 55^{\circ}$; (b) an illustration of the movement of the frame; (c) the deformed fabric from the picture frame test simulation.

The sheared fabric from the picture frame test is shown in Fig. 5 (a), which is not strictly consistent for all the samples. Wrinkles may appear at the arm regions of some samples, but the center region always stays flat. The phenomenon is consistent with the simulation results shown in Fig. 5 (c). Note that the wrinkling at the arm region predicted from simulation is still in small magnitude. The shear responses during the picture frame tests are demonstrated in Fig. 6 and 7. The shear force was normalized, and it can be computed from the measured force $F_{measured}$ and half of the angle between the weft and warp tows θ , according to Eqs. 52-53. The normalization excludes the effect of the frame and fabric sizes as indicated in Cao's work and makes the responses more representative for the carbon fabric materials [36,38].

$$F_{normalized} = F_{shear} \cdot \frac{L_{frame}}{L_{fabric}^2} \tag{52}$$

$$F_{shear} = \frac{F_{measured}}{2\cos\theta} \tag{53}$$

At the initial stage of Fig. 6, the normalized shear force is increasing almost linearly with the shear angle at a small slope. This is because when the shear angle is small, there are large channels between fiber tows, and the rotation of the warp and weft yarns dominates the deformation. The inter-tow friction mainly contributes to the shear force while the intra-tow friction can also be involved. Then, as the channels gradually close, the inter-tow rotation is limited and the compaction from neighboring yarns causes a sudden growth in the shear force near a shear locking angle. In this study, the locking angle is around 55°. After the locking, the shear force increases linearly again with the shear angle with larger stiffness. When the crosshead stops moving, the normalized shear force first decreases drastically from its maxima within several seconds (see Fig. 7). Then, as most of the viscous energy has been dissipated, the normalized shear force tends to stabilize.

2. An in-plane shear model

A picture frame test model was implemented in Abaqus. The model consists of a rigid frame and a piece of fabric identical in size to the real ones. Each frame bar was created as a 5 mm wide plate with an elastic modulus of 10^9 MPa. which is much larger than the modulus of fibers to prevent the deformation of the frame. The frame bars were pinned at the ends. The fabric was created as a solid plate of 0.25 mm thick, and it was pinned to the frame. The bottom left corner of the frame was fixed. The top right corner was moved at 35 mm/min at 45° with respect to x-axis for 96mm in 2.75 minutes. The deformed fabric predicted by the simulation is shown in Fig. 5(c). The material properties were characterized by comparing the normalized shear force vs. shear angle responses and the history of the normalized shear force obtained from the simulations and the experiments as shown in Fig. 6 and 7. Generally, the in-plane shear properties shown in Table 2 have managed to achieve predicted shear responses close to the experimental results.

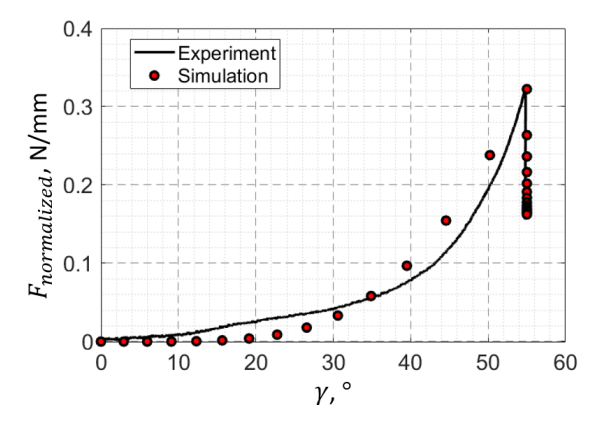


Fig. 6 The normalized shear force vs. shear angle responses obtained from the picture frame shear experiment and simulation.

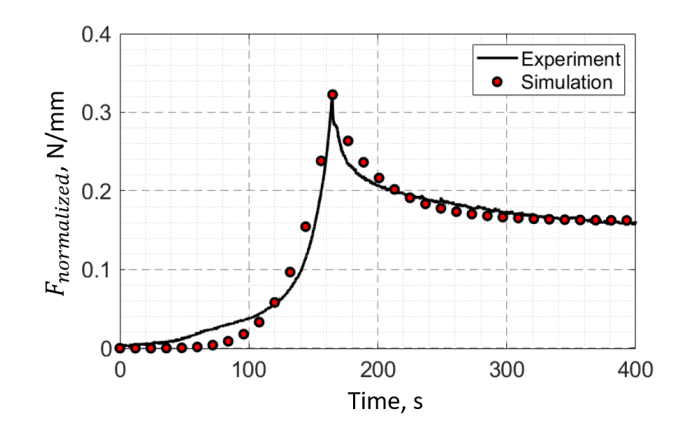


Fig. 7 The normalized shear force vs. time responses obtained from the picture frame shear experiment and simulation.

Table 2. Material properties that control the in-plane shear behavior

E_s (MPa)	n	$\boldsymbol{\beta}_s$	τ_s (min)
0.185	6	1.7	0.6

C. Through-Thickness Compaction Behaviors

To characterize the through-thickness compaction properties, compaction tests were conducted, and a corresponding model was built in Abaqus. Again, the material properties were calibrated to match the reaction force response measured from the experiments.

1. Through-thickness compaction experiments

The setup for the compression tests is shown in Fig. 8 (a). The area of the tool plates is $2.8'' \times 2.8''$. Four plies of fabrics in $2.5'' \times 2.5''$ were cut and stacked together. Before the test, the upper and lower molds were around 6.5 mm away from one another. As the test started, the lower grip moved towards the upper grip at 0.5mm/s for 6mm. After the ramp, the position of the grip was held constant for 10 minutes. Again, force, displacements, and time were recorded from the very beginning and are plotted in Fig. 9 (a). Clearly, the process is divided into three stages by the positions where the force starts to increase, d_1 , and where the increase stops, d_2 , as marked by dash lines: (1) the nocontact stage, (2) the increased compression stage, and (3) the relaxation stage. At first, the mold is not in contact with the fabrics, leading to zero reaction force. Then, the force grows linearly with time (also with displacements) as the compression happens. Finally, it drops due to stress relaxation. The duration of the second stage was measured to be 1.006 s. The displacement of the crosshead during this stage is computed as

$$d = d_2 - d_1 = 0.493 \, mm \tag{54}$$

The data will be used as the boundary conditions of the compaction simulation.

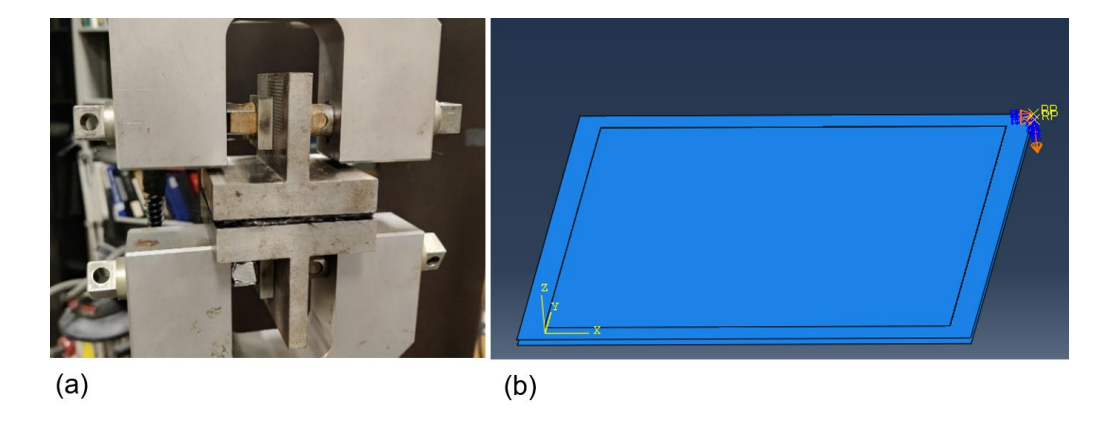


Fig. 8 (a) The compaction test setup; (b) the compaction model in Abaqus.

2. A through-thickness compaction model

A compaction model was built in Abaqus shown in Fig. 8 (b). Two tool plates were created as analytical rigid shells controlled by reference points. Each fabric layer was modelled as a 0.25mm thick solid plate, and four layers were stacked together. Contact pairs were assigned between two adjacent fabric sheets as well as between fabrics and tools. The contact properties include the "hard" normal interaction behavior and the penalty friction transverse interaction behavior with a commonly used friction coefficient of 0.3 [14]. Initially, the upper tool plate was in contact with the upper-most surface of fabrics and the lower tool plate touched the lower-most surface of fabrics without compression. In the first step, the upper plate moved towards the lower plate at a constant speed for 0.493mm in one second, followed by a dwell time of one minute. The material properties that control the compaction behaviors were tuned until the reaction force RF3 vs. time responses output from Abaqus showed good agreement with the experimental curve, as shown in Fig. 9 (b). The characterized properties are shown in Table 3.

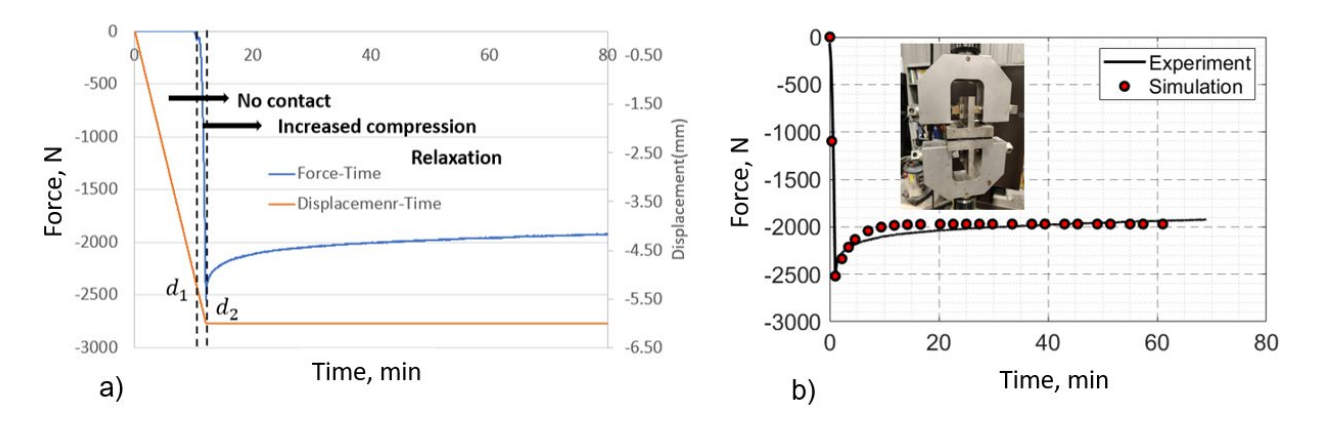


Fig. 9 (a) The force vs. time and displacement vs. time responses obtained from the compaction experiment; (b) the force vs. time responses from the compaction experiment and simulation.

Table 3. Material properties that control the through-thickness compaction behavior

E_t (MPa)	$oldsymbol{eta}_t$	τ_t (min)
0.85	0.33	0.05

IV. Model Validation

The proposed hyper-viscoelastic modeling approach is validated in this section. A hemisphere draping test was carried out and a corresponding model was implemented in Abaqus. The deformed shape, shear angles, and force responses predicted from the simulation were compared to those from the draping experiments.

A. Draping Experiment

The setup of hemisphere draping tools is shown diagrammatically in Fig. 10. A set of aluminum frame and die support were connected to the upper grip of a test machine. A metal punch of diameter 152.4 mm (6'') was connected to the lower grip of the tension machine. One acrylic blank holder was placed on top of the die support. Holes of diameter 160 mm were cut in the center of the die support and blank holder to enable the punch to go though. All the surfaces that would be in contact with fabrics were polished and treated with lubricant to reduce friction.

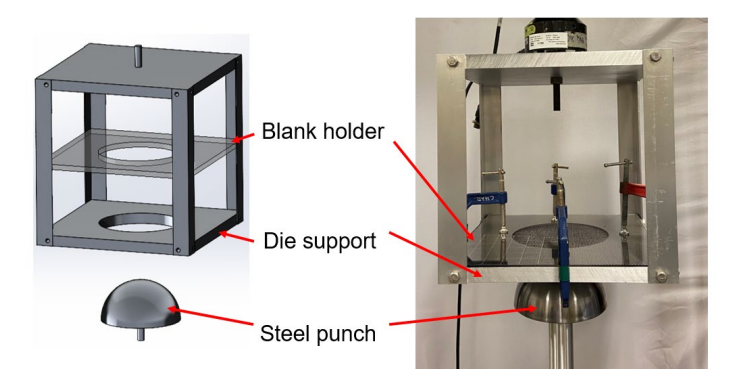


Fig. 10 The setup of hemisphere draping test.

Before the test began, four plies of T300 carbon fiber reinforced plain-weave fabric samples were stacked one upon another to form a four-ply assembly. Take the directions along the edges of the frame as x-y-z coordinates. The fiber directions are along 0° and 90°, denoted as 1 and 2 directions. A 3 cm grid was drawn on the top layer. Then, the fabrics were placed on the die support and pressed by the blank holder. Translucent tape was applied to connect the blank holder and die support. The punch was raised to touch the bottom of the fabrics. Then, the fabric was draped upwards for 65 mm in one minute with a constant speed. Pictures were taken from the top view through the transparent blank holder to record the deformed shapes of fabrics. Three tests were conducted for each type.

The deformed fabrics are shown in Fig. 11. No wrinkling was clearly observed in most cases. Fiber sliding did not occur in the center area but only slightly at the edges where fiber tows can be easily peeled away by friction. Shear angles are large along the diagonal line $(\pm 45^{\circ})$ and are almost zero along the midlines (0°) and (0°) . The angle reaches maximum near the end of the dome and decreases along the diagonal line from the apex to the end of the dome. Moreover, the shear angle also decreases from the end of the dome to the corner of the fabrics. Angles between the warp and weft tows at six points were measured from the pictures and recorded in Table 4.

The force vs. time response is shown in Fig. 12. The reaction force has similar magnitude and trend. The force first grows nonlinearly with time and decreases when the punch stops moving.

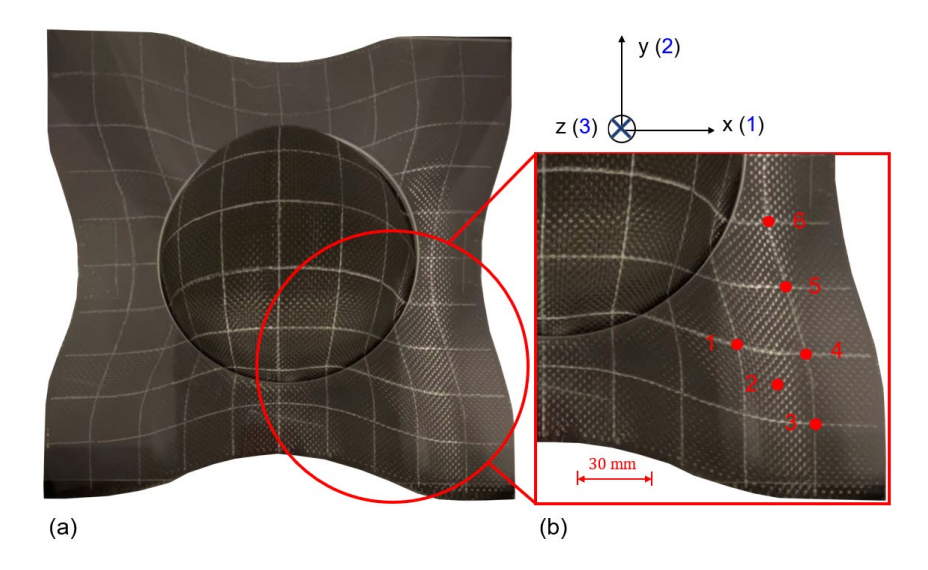


Fig. 11 (a) The deformed 0/90° fabrics after the hemisphere draping test; (b) the six points where the angles between the warp and weft tows were measured.

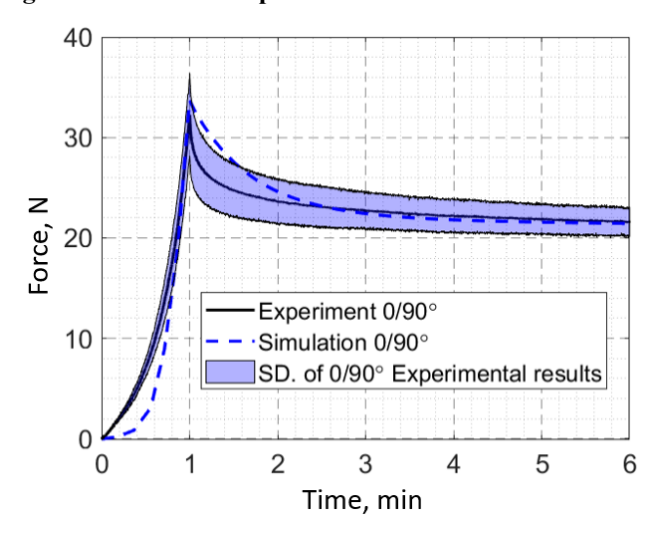


Fig. 12 The reaction force vs. time responses from the draping experiments for $0/90^{\circ}$ fabrics. The experimental results are obtained from three hemisphere draping tests.

B. Draping Simulation

A hemisphere draping simulation was implemented in Abaqus using the dynamic implicit solver for T300 carbon plain-weave fabrics. Fig. 13 shows the setup in the model. The blank holder and die support were created as one rigid part (called as BHDS hereinafter). The punch was also modeled as a rigid body mastered by a reference point. Four layers of identical fabric plies were stacked along the z-direction but only a quarter of the assembly was included in the model (150mm×150mm) with symmetric boundary conditions imposed at two edges. Initially, the BHDS is in contact with the upper and lower surfaces of the fabrics without compression. The BHDS is fixed during the whole process, and the punch moves down for 65 mm in one minute, followed by dwell for five minutes. The mesh size was 3 mm. Contact pairs were identified between the surfaces that could be in contact, and the penalty method was used for tangential interaction behavior. The friction coefficient between fabric-fabric surfaces is 0.3. The authors have tested the inter-ply friction from 0.1 to 0.5, but the results are consistent, indicating that the inter-ply sliding is not a major deformation mode during the draping process. The friction coefficient of the fabric-tool contact is reduced to 0.044 [39], since the oil-based lubricant was thoroughly applied to the tool surfaces.

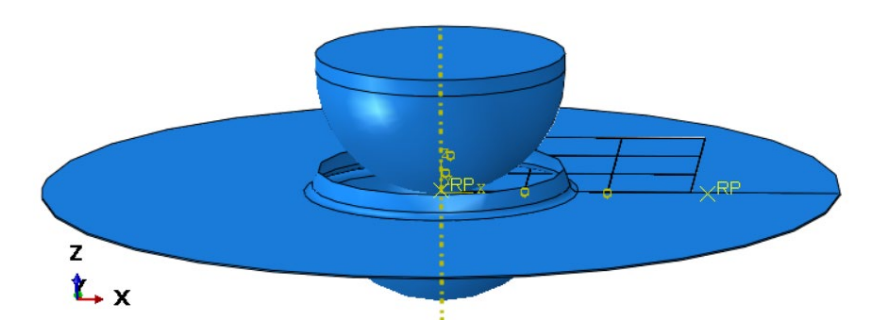


Fig. 13 The hemisphere draping model in Abaqus.

The deformed shape and Lagrangian shear strain (LE12) are shown in Fig. 14. Similar to the draped fabrics in the experiments, no out-of-plane wrinkle shows up. The fabrics deform the most along the midlines. The draping force exerted by the punch compels the fabrics that sit on the die support to move radially towards the center of the hole. Therefore, the moving directions of the inextensible fiber tows at the midlines align with their axial directions, resulting in large translation rather than in-plane rotation of fiber tows. The predicted shear angles show a very similar trend to those in the experiments. Along the diagonal line, the shear angle first increases from zero and then decreases back to zero from the bottom-left corner to the top-right corner of the fabrics in Fig. 14. The deformed shapes before and after the relaxation indicate that the energy dissipation only exerts distinct influence on the compaction force, rather than fabric deformation during the hemisphere draping process.

The angles between the warp and weft tows from the same points as those in experiments were measured and shown in Table 4. The relative error between simulation results and experiment results were calculated as

$$Relative error = \frac{\gamma_{simulation} - \gamma_{experiment}}{\gamma_{experiment}}$$
 (54)

Generally speaking, the predicted shear angles are in a good agreement with experiment results with small errors (<5%). Possibly, the errors come from the measurements and the uncertainty involved in the real experiments.

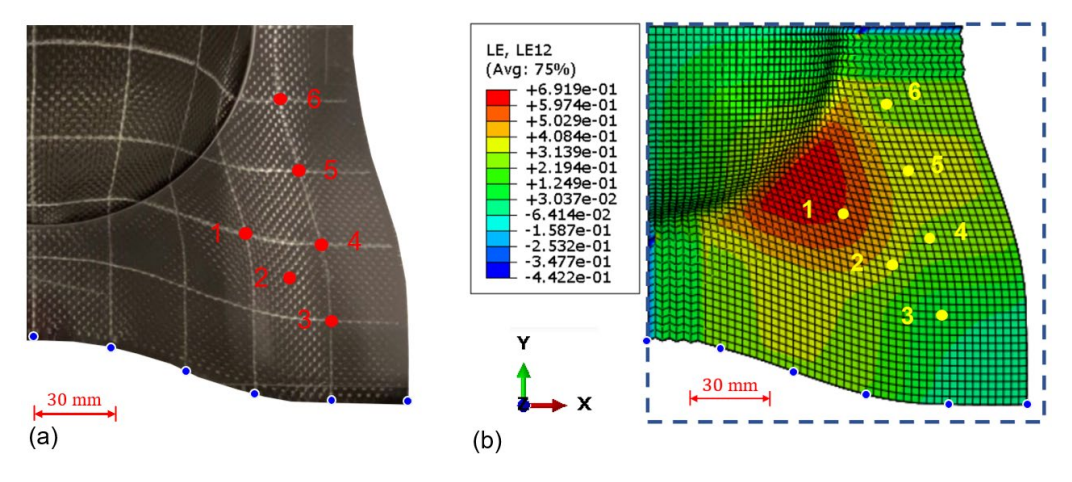


Fig. 14 The shear strain (LE12) distribution of the fabrics predicted by the hemisphere draping model after the process is fully completed

Table 4. The angles between the warp and weft tows from the experiment results and simulation results together with their relative errors for 0/90° fabric

Point	1	2	3	4	5	6
Experiment	51.71°	71.43°	86.60°	71.78°	68.85°	76.23°
Simulation	53.67°	70.99°	87.47°	75.20°	69.39°	73.54°
Relative error	3.79%	-0.62%	1.00%	4.76%	0.78%	-3.53%

The reaction force of the BHDS vs. time response from the simulations is shown in Fig. 12. Generally, it is close to the experimental curves. The largest deviation shows up at the start of the draping process. This is mainly caused by the error from the characterization of in-plane shear properties. The shear modulus was underestimated in the initial shearing stage to maintain the good accuracy of fitting during the whole shearing process. The bending and compaction properties exert less influence on the reaction force, compared to shear properties, since the distance between the blank holder and die support is fixed during the simulation, which is slightly different from the real boundary conditions in the experiments. In addition, the uncertainties of the fabric samples and the boundary conditions during the shear, bending, compaction, and draping experiments can also affect the experimental results. In conclusion, the good agreement between the experimental and simulation results demonstrates that the proposed modeling methodology works well in the prediction of the fabric deformations and the applied force.

V. Conclusion

This paper puts forward a new hyper-viscoelastic model for textile woven dry fabrics based on the development of an SEDF. Nonequilibrium stresses are considered and updated according to a Maxwell model made of one elastic arm and one Maxwell arm. The bending, in-plane shear, and through-thickness normal behaviors were characterized by cantilever beam bending, picture frame shear and compaction tests, respectively. The relaxation behaviors of fabrics were successfully captured by having dwell periods in experiments and adjusting β_{α} and τ_{α} in the corresponding models to make the predicted and measured responses coincident. The proposed method was applied to examples of the hemisphere draping simulation in Abaqus. The good agreement between the experiment results and simulation results validates the capability of the proposed method to capture the fabric deformations and applied force when the fabrics are draped by a mold with complex geometry in LCM.

Acknowledgments

The authors are grateful for the support of the National Science Foundation under Grant No. 2105448. We also thank Mr. Yao Sun at Purdue University for his assistance in manufacturing the testing tools.

References

- [1] Heardman, E., Lekakou, C., and Bader, M. G. "In-Plane Permeability of Sheared Fabrics." *Composites Part A: Applied Science and Manufacturing*, Vol. 32, No. 7, 2001, pp. 933–940. https://doi.org/10.1016/S1359-835X(01)00006-9.
- [2] Pantaloni, D., Bourmaud, A., Baley, C., Clifford, M. J., Ramage, M. H., and Shah, D. U. "A Review of Permeability and Flow Simulation for Liquid Composite Moulding of Plant Fibre Composites." *Materials*, Vol. 13, No. 21, 2020, p. 4811. https://doi.org/10.3390/ma13214811.
- [3] Chen, Z., Pan, S., Zhou, Z., Lei, T., Dong, B., and Xu, P. "The Effect of Shear Deformation on Permeability of 2.5D Woven Preform." *Materials*, Vol. 12, No. 21, 2019, p. 3594. https://doi.org/10.3390/ma12213594.
- [4] Rudd, C. D., Long, A. C., McGeehin, P., and Smith, P. "In-Plane Permeability Determination for Simulation of Liquid Composite Molding of Complex Shapes." *Polymer Composites*, Vol. 17, No. 1, 1996, pp. 52–59. https://doi.org/10.1002/pc.10590.
- [5] Boisse, P., Colmars, J., Hamila, N., Naouar, N., and Steer, Q. "Bending and Wrinkling of Composite Fiber Preforms and Prepregs. A Review and New Developments in the Draping Simulations." *Composites Part B: Engineering*, Vol. 141, 2018, pp. 234–249. https://doi.org/10.1016/j.compositesb.2017.12.061.
- [6] Sjölander, J., Hallander, P., and Åkermo, M. "Forming Induced Wrinkling of Composite Laminates: A Numerical Study on Wrinkling Mechanisms." *Composites Part A: Applied Science and Manufacturing*, Vol. 81, 2016, pp. 41–51. https://doi.org/10.1016/j.compositesa.2015.10.012.
- [7] Hallander, P., Sjölander, J., and Åkermo, M. "Forming Induced Wrinkling of Composite Laminates with Mixed Ply Material Properties; an Experimental Study." *Composites Part A: Applied Science and Manufacturing*, Vol. 78, 2015, pp. 234–245. https://doi.org/10.1016/j.compositesa.2015.08.025.

- [8] Boisse, P., Hamila, N., Vidal-Sallé, E., and Dumont, F. "Simulation of Wrinkling during Textile Composite Reinforcement Forming. Influence of Tensile, in-Plane Shear and Bending Stiffnesses." *Composites Science and Technology*, Vol. 71, No. 5, 2011, pp. 683–692. https://doi.org/10.1016/j.compscitech.2011.01.011.
- [9] Wang, Y., and Sun, X. "Digital-Element Simulation of Textile Processes." Composites Science and Technology, Vol. 61, No. 2, 2001, pp. 311–319. https://doi.org/10.1016/S0266-3538(00)00223-2.
- [10] Zhou, G., Sun, X., and Wang, Y. "Multi-Chain Digital Element Analysis in Textile Mechanics." Composites Science and Technology, Vol. 64, No. 2, 2004, pp. 239–244. https://doi.org/10.1016/S0266-3538(03)00258-6.
- [11] Khan, H. A., Hassan, A., Saeed, M. B., Mazhar, F., and Chaudhary, I. A. "Finite Element Analysis of Mechanical Properties of Woven Composites Through a Micromechanics Model." *Science and Engineering of Composite Materials*, Vol. 24, No. 1, 2017, pp. 87–99. https://doi.org/10.1515/secm-2014-0266.
- [12] Lin, H., Clifford, M. J., Long, A. C., and Sherburn, M. "Finite Element Modelling of Fabric Shear." Modelling and Simulation in Materials Science and Engineering, Vol. 17, No. 1, 2009, p. 015008. https://doi.org/10.1088/0965-0393/17/1/015008.
- [13] Kaka, D., Rongong, J. A., Hodzic, A., and Lord, C. Dynamic Mechanical Properties of Woven Carbon Fibre Reinforced Thermoplastic Composite Materials. 2015.
- [14] Gatouillat, S., Bareggi, A., Vidal-Sallé, E., and Boisse, P. "Meso Modelling for Composite Preform Shaping Simulation of the Loss of Cohesion of the Woven Fibre Network." *Composites Part A: Applied Science and Manufacturing*, Vol. 54, 2013, pp. 135–144. https://doi.org/10.1016/j.compositesa.2013.07.010.
- [15] Faccio Júnior, C. J., and Gay Neto, A. "Challenges in Representing the Biaxial Mechanical Behavior of Woven Fabrics Modeled by Beam Finite Elements With Contact." *Composite Structures*, Vol. 257, 2021, p. 113330. https://doi.org/10.1016/j.compstruct.2020.113330.
- [16] Saito, M., and Neto, A. Woven Fabrics Computational Simulation Using Beam-to-Beam Contacts Formulation. 2016.
- [17] Nguyen, Q. T., Gomes, A. J. P., and Ferreira, F. B. N. "Buckling Analysis of Plain-Woven Fabric Structure Using Shell Element and a One Cell-Based Integration Scheme in Smoothed Finite Element Method." *IOP Conference Series:* Materials Science and Engineering, Vol. 459, 2018, p. 012055. https://doi.org/10.1088/1757-899X/459/1/012055.
- [18] Bai, R., Colmars, J., Chen, B., Naouar, N., and Boisse, P. "The Fibrous Shell Approach for the Simulation of Composite Draping With a Relevant Orientation of the Normals." *Composite Structures*, Vol. 285, 2022, p. 115202. https://doi.org/10.1016/j.compstruct.2022.115202.
- [19] Charmetant, A., Orliac, J. G., Vidal-Sallé, E., and Boisse, P. "Hyperelastic Model for Large Deformation Analyses of 3D Interlock Composite Preforms." Composites Science and Technology, Vol. 72, No. 12, 2012, pp. 1352–1360. https://doi.org/10.1016/j.compscitech.2012.05.006.
- [20] Peng, X., Guo, Z., Du, T., and Yu, W.-R. "A Simple Anisotropic Hyperelastic Constitutive Model for Textile Fabrics With Application to Forming Simulation." *Composites Part B: Engineering*, Vol. 52, 2013, pp. 275–281. https://doi.org/10.1016/j.compositesb.2013.04.014.
- [21] Mathieu, S., Hamila, N., Bouillon, F., and Boisse, P. "Enhanced Modeling of 3D Composite Preform Deformations Taking Into Account Local Fiber Bending Stiffness." *Composites Science and Technology*, Vol. 117, 2015, pp. 322–333. https://doi.org/10.1016/j.compscitech.2015.07.005.
- [22] Cusick, G. E. "46—THE DEPENDENCE OF FABRIC DRAPE ON BENDING AND SHEAR STIFFNESS." *Journal of the Textile Institute Transactions*, Vol. 56, No. 11, 1965, pp. T596–T606. https://doi.org/10.1080/19447026508662319.
- [23] Sharma, S. B., Sutcliffe, M. P. F., and Chang, S. H. "Characterisation of Material Properties for Draping of Dry Woven Composite Material." *Composites Part A: Applied Science and Manufacturing*, Vol. 34, No. 12, 2003, pp. 1167–1175. https://doi.org/10.1016/j.compositesa.2003.09.001.
- [24] Dong, L., Lekakou, C., and Bader, M. G. "Solid-Mechanics Finite Element Simulations of the Draping of Fabrics: A Sensitivity Analysis." Composites Part A: Applied Science and Manufacturing, Vol. 31, No. 7, 2000, pp. 639–652. https://doi.org/10.1016/S1359-835X(00)00046-4.
- [25] Wang, X., Liu, X., and Deakin, C. H. Physical and Mechanical Testing of Textiles. In *Fabric Testing*, Elsevier, 2008, pp. 90–124.
- [26] Nguyen, N., and Waas, A. M. "Nonlinear, Finite Deformation, Finite Element Analysis." Zeitschrift für angewandte Mathematik und Physik, Vol. 67, No. 3, 2016, p. 35. https://doi.org/10.1007/s00033-016-0623-5.
- [27] Holzapfel, G. A. "Nonlinear Solid Mechanics: A Continuum Approach for Engineering Science." Meccanica, Vol. 37, No. 4/5, 2002, pp. 489–490. https://doi.org/10.1023/A:1020843529530.
- [28] Sun, H., and Pan, N. "Shear Deformation Analysis for Woven Fabrics." *Composite Structures*, Vol. 67, No. 3, 2005, pp. 317–322. https://doi.org/10.1016/j.compstruct.2004.01.013.
- [29] Taha, I., Abdin, Y., and Ebeid, S. "Comparison of Picture Frame and Bias-Extension Tests for the Characterization of Shear Behaviour in Natural Fibre Woven Fabrics." *Fibers and Polymers*, Vol. 14, No. 2, 2013, pp. 338–344. https://doi.org/10.1007/s12221-013-0338-6.
- [30] Shen, H., Wang, P., and Legrand, X. "In-Plane Shear Characteristics During the Forming of Tufted Carbon Woven Fabrics." *Composites Part A: Applied Science and Manufacturing*, Vol. 141, 2021, p. 106196. https://doi.org/10.1016/j.compositesa.2020.106196.
- [31] Lindberg, J., Behre, B., and Dahlberg, B. "Part III: Shearing and Buckling of Various Commercial Fabrics." *Textile Research Journal*, Vol. 31, No. 2, 1961, pp. 99–122. https://doi.org/10.1177/004051756103100203.

- [32] Dinh, T., Daelemans, L., and van Paepegem, W. Near-Microscale Modelling of Dry Woven Fabrics Under In-Plane Shear Loading. 2019.
- [33] Wang, Y., Zhang, W., Ren, H., Huang, Z., Geng, F., Li, Y., and Zhu, Z. "An Analytical Model for the Tension-Shear Coupling of Woven Fabrics with Different Weave Patterns under Large Shear Deformation." *Applied Sciences*, Vol. 10, No. 4, 2020, p. 1551. https://doi.org/10.3390/app10041551.
- [34] Mohammed, U., Lekakou, C., Dong, L., and Bader, M. G. "Shear Deformation and Micromechanics of Woven Fabrics." *Composites Part A: Applied Science and Manufacturing*, Vol. 31, No. 4, 2000, pp. 299–308. https://doi.org/10.1016/S1359-835X(99)00081-0.
- [35] Habboush, A., Sanbhal, N., Shao, H., Jiang, J., and Chen, N. "Characterization and Analysis of In-Plane Shear Behavior of Glass Warp-Knitted Non-Crimp Fabrics Based on Picture Frame Method." *Materials*, Vol. 11, No. 9, 2018, p. 1550. https://doi.org/10.3390/ma11091550.
- [36] Cao, J., Akkerman, R., Boisse, P., Chen, J., Cheng, H. S., de Graaf, E. F., Gorczyca, J. L., Harrison, P., Hivet, G., Launay, J., Lee, W., Liu, L., Lomov, S. V., Long, A., de Luycker, E., Morestin, F., Padvoiskis, J., Peng, X. Q., Sherwood, J., Stoilova, Tz., Tao, X. M., Verpoest, I., Willems, A., Wiggers, J., Yu, T. X., and Zhu, B. "Characterization of Mechanical Behavior of Woven Fabrics: Experimental Methods and Benchmark Results." *Composites Part A: Applied Science and Manufacturing*, Vol. 39, No. 6, 2008, pp. 1037–1053. https://doi.org/10.1016/j.compositesa.2008.02.016.
- [37] Boisse, P., Hamila, N., Guzman-Maldonado, E., Madeo, A., Hivet, G., and dell'Isola, F. "The Bias-Extension Test for the Analysis of In-Plane Shear Properties of Textile Composite Reinforcements and Prepregs: A Review." *International Journal of Material Forming*, Vol. 10, No. 4, 2017, pp. 473–492. https://doi.org/10.1007/s12289-016-1294-7.
- [38] Peng, X. Q., Cao, J., Chen, J., Xue, P., Lussier, D. S., and Liu, L. "Experimental and Numerical Analysis on Normalization of Picture Frame Tests for Composite Materials." *Composites Science and Technology*, Vol. 64, No. 1, 2004, pp. 11–21. https://doi.org/10.1016/S0266-3538(03)00202-1.
- [39] Tortora, A. M., and Halenahally Veeregowda, D. "True Stability of Lubricants Determined Using the Ball-on-Disk Test." Advances in Tribology, Vol. 2016, 2016, pp. 1–6. https://doi.org/10.1155/2016/4020537.